Millimeter and Sub-millimeter Wave Transmission Through a Radome Covered by Water: The Impact of the Shape of Water

Paul Bouquin, Daniel Bourreau, Alain Peden

Noname manuscript No.
(will be inserted by the editor)

Millimeter and Sub-millimeter Wave Transmission Through a Radome Covered by Water : the Impact of the Shape of Water

Paul Bouquin[1], Daniel Bourreau[1], Alain Peden[1]

Received: date / Accepted: date

Abstract Rainfall can reduce the radar signal through a radome. The effects of different water layers on the radome transmission is studied using quasi-optical measurement from 26 to 330 GHz including water permittivity characterization. The water is deposited as drops of different sizes or as a uniform layer while keeping a constant volume, highlighting the importance of the control of the total wet surface for radar applications. A compact model is proposed to predict the signal loss due to water on the radome depending on the rain flow.

Keywords millimeter waves · sub-THz · free-space · radome · rain

1 Introduction

Nowadays, many applications make use of the mm-wave and low THz bands [1,2]. When operating in the outside environment, the system antennas must be protected from water splashes, rain, dust and dirt by a radome, or hidden for aesthetic and aerodynamic reasons with technical issues. This is the case for instance of the automotive radar working currently at 77 GHz [3,4] and projecting to go further up in frequency [5], or wireless back-haul for 5G applications where radome can also help to customize antenna radiation pattern [6].

During a rainfall event, the water between the transmitter and the receiver or the radar and the target is going to absorb a part of the propagating wave while the water accumulated on the radome surface forms a nontransparent layer just in front of the transceiver or radar antenna [7,8]. This can be especially detrimental for automotive applications with impaired performances (detection range, false detection,...) of automotive sensors under adverse weather conditions as we advance towards autonomous vehicles [3].

[1]Lab-STICC, UMR 6285 CNRS, IMT Atlantique, technopôle Brest-Iroise, CS 83818, 29238 Brest Cedex 3

The type of water flow varies with the hydrophobicity of the radome surface, its tilt angle and the rain intensity. For a low rain intensity or a highly hydrophobic surface, the water forms thin rivulets, while an heavy rainfall on a degraded surface can flow in a laminar fashion [9]. For this reason, under the same rain intensity, the signal is further impacted if the hydrophobic surface is damaged [10]. In order to mimic a laminar flow or a rivulet flow, water has been deposited as drops or as a uniform layer on a radome using free-space method characterization[11]. In [12] and [13], it was shown that water has a lesser impact on the signal in the case of drops as compared to a uniform layer. However, experimental characterization was limited in frequency range and in the control of the water layer, the thickness or permittivity of water not being accurately known.

The aim of this study is to characterise a radome covered by a water layer in different shapes. Measurements of the S-parameters of a wet radome are performed using quasi-optical free-space test benches for a large frequency band coverage, from 26 GHz up to 330 GHz. The permittivity of water was also extracted from S-parameter measurements of a specific container filled with water and its frequency variation fitted by a Debye model. The water is then deposited on the radome in three different shapes: small droplets, larger drops and a uniform layer. These three water layer shapes aim to mimic the different types of flow during a rainfall event. The thin water film is obtained through a new method allowing us to get a good control of this thickness, so that the same volume of water for the three shapes can be kept. Finally, a model is proposed to take into account the total surface covered by water and to predict the total loss of signal due to the water layer.

The paper is organized as follows. The experimental setups for S-parameter measurements are presented in Section II. Section III describes the method for controlling the shape of water. The characterization of the different water layers is presented in Section IV and discussion on the measurement results in Section V. A compact model for transmission loss through water layers is proposed in Section VI and conclusion and future works are given in Section VII.

2 Experimental set-up for permittivity extraction

2.1 Experimental set-up implementation

Three different quasi-optical test benches are implemented in the Ka (26 to 40 GHz), W (75 to 110 GHz) and J (220 to 330 GHz) bands. Two of them can be operating at the same time (Ka and W or J). The principle in each frequency band is the same : a vector network analyser (VNA) in a 2-port configuration produces a signal which is converted in the millimeter wave range which then goes through a corrugated horn antenna and a gaussian lens. These two elements form a GOLA (Gaussian Optics Lens Antenna) to propagate the electromagnetic wave in free space as a gaussian beam. For each normalized

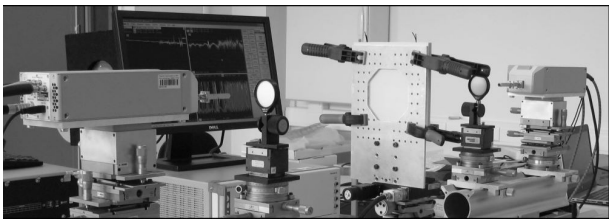

Fig. 1 The quasi-optical set-up in the J band: the frequency converters, the lens and the sample holder are aligned on a rail. The material under test is held in place by clamps.

frequency band, specific designed GOLAs are used as well as dedicated frequency converters. In between the GOLAs, the sample under study is placed on its holder at the waist of the gaussian beam (see Fig. 1). The GOLA is designed to create a focused or a paraxial beam, depending on the ratio between the waist and the wavelength [14]. The higher the ratio, the more paraxial the beam. A highly paraxial beam is required so that the sample position between the two GOLAs is not critical and the plane wave assumption can be used. Therefore, the S-parameter measurement can be performed without filtering nor time gating. The gaussian beam waist radius is about 6 cm at 30 GHz, 3 cm at 90 GHz and 2 cm at 250 GHz. The sample must be always larger than this radius to avoid edge effects.

To measure the four S-parameters of the sample, a free-space Thru-Reflect-Line (TRL) calibration must be performed to ensure an accurate location of the reference plane using the following procedure. After a preliminary TRL calibration done at the waveguide flanges (i.e. without the GOLAs), the most accurate alignment of the GOLAs can be achieved by maximizing the signal transmission between them. Once the antennas are positioned, the free-space calibration is performed: an Aluminium-metal plate is used as the reflect standard, the GOLA at port 2 is moved away for the line standard (about a quarter wavelength at the midd-band) and moved back for the Thru. A new free-space TRL calibration is repeated before each set of measurements. As previously mentioned, no smoothing or time-domain gating is applied to the measured data. The W band set-up and the characterization method for a solid material are described in [15].

Under the plane-wave assumption and normal incidence, the **S** matrix of a uniform dielectric slab with parallel faces is given by [16]:

$$S_{21} = S_{12} = \frac{(1-\rho^2)\exp(-\mathrm{j}\beta h)}{1-\rho^2\exp(-2\mathrm{j}\beta h)} \tag{1}$$

$$S_{11} = S_{22} = \frac{\rho(1-\exp(-2\mathrm{j}\beta h))}{1-\rho^2\exp(-2\mathrm{j}\beta h)} \tag{2}$$

with

$$\rho = \frac{1-\sqrt{\epsilon_\mathrm{r}}}{1+\sqrt{\epsilon_\mathrm{r}}},\ \beta = \frac{2\pi}{\lambda}\sqrt{\epsilon_\mathrm{r}}$$

where h is the thickness of the slab and $\epsilon_{\mathrm{r}} = \epsilon'_{\mathrm{r}} - j\epsilon''_{\mathrm{r}}$ its complex relative permittivity. By comparing the measured **S** matrix with the above equations, the complex permittivity at each frequency point can be extracted using S_{21} or S_{12} while the thickness h of the slab is adjusted by matching S_{11} and S_{22} as explained in [15].

2.2 Permittivity extraction

Throughout this study, the radome is a piece of PVC which was characterized in each frequency band. Its extracted relative complex permittivity and associated thickness are:

$$\epsilon_{\mathrm{r}} = 2.956 - \mathrm{j}(0.0044 + 0.00023 f(\mathrm{GHz}))$$

$$h = 5.01 \text{ mm}$$

The dispersion of the real part of the permittivity is negligible (less than 1 %), but the dispersion of the imaginary part must be taken into account given the wide frequency range from the Ka up to J band. It can be well fitted with a linear function.

To extract the complex permittivity of water, a PVC container was used. First, each panel of the container is separately characterized using the previous procedure, then the empty container and filled with water are measured. The permittivity of the non-solid material is obtained by comparing the measured and calculated **S** matrix of the container filled with water. The calculated **S** matrix is given by (1) and (2) and by the **S**-to-**T** matrix transformation described in the appendix. The empty container measurement gives the exact thickness of the liquid under study because the air permittivity is known. The full protocol to extract the permittivity of a non-solid material is detailed in reference [17].

In the present study, we use tap water which is is let in the open air a couple of days for the chlorine to be evaporated. The permittivity of water is extracted simultaneously in the Ka and J bands and measurements are compared to a 3-term Debye model given by [18]:

$$\epsilon_{\mathrm{r,eau}} = \epsilon_{\mathrm{r},\infty} + \frac{\epsilon_{\mathrm{r},0} - \epsilon_{\mathrm{r},\infty}}{1 + \mathrm{j}2\pi f\tau} \tag{3}$$

A very good match with the measurements from the Ka to J band is obtained with the following parameters:

$$\epsilon_{\mathrm{r},0} = 86.5$$

$$\epsilon_{\mathrm{r},\infty} = 5.83$$

$$\tau = 7.51 \text{ ps}$$

As depicted in Fig. 2, the model in the W band does not fit exactly the imaginary part of the measured permittivity. As only two quasi-optical setups

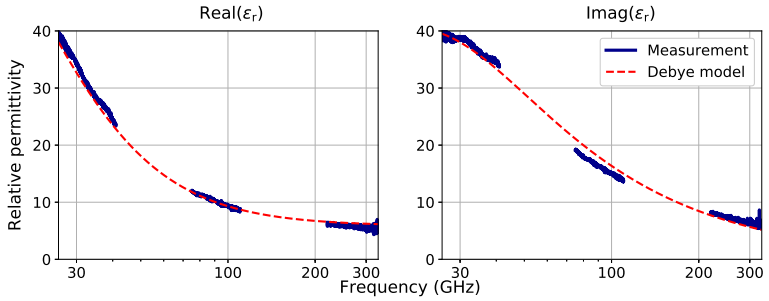

Fig. 2 Complex relative permittivity of water versus frequency. The measurements are performed in the Ka, W and J band. Red dashed-line : Debye model with three free parameters adjusted to the measurements (eq.3).

can be operated at the same time, the tap water was characterized simultaneously in the Ka and J band at a room temperature of 29 degrees, while the room temperature was about 22 degrees for the W-band measurements. The temperature has a strong impact on the permittivity of water as shown in [18].

3 Methods for controlling and characterizing the shape of water

3.1 Shapes of water

When the rain falls on the radome, the total surface covered by water depends on the hydrophobicity of the material. The higher the hydrophobicity, the lesser the total surface covered by water as the rivulets grow thinner. For non hydrophobic surfaces with heavy rainfall, a thin film of water can appear as a laminar flow. In this study, rain is not falling on the radome but a fixed volume of water is deposited in different manners to study the impact of the total percent of wet surface, written α. The steps of the procedure are described hereinafter: i) droplets are deposited on the radome using a spray, ii) the water is then collected and deposited randomly as large drops using a syringe, iii) the water is collected again and deposited as a thin film using a polycarbonate plate to flatten it and double side adhesive tape as a seal (see Fig. 3.a). Pictures of the obtained water shapes are shown in Fig. 4.a. A fixed surface of 80 cm^2 is delimited with the tape. The total volume of water is 0.8 mL. Up to 10 % of the volume can be lost due to evaporation or other losses between each step. The measured radius of the droplets using a microscope is between 0.05 and 2 mm. To estimate the total percent of the surface covered by water, we add coloring to the water and process the resulting picture: $\alpha_{\text{droplets}} = (40 \pm 10)$ %. The larger drops have a much tighter radius distribution with an average of 1.75 mm. On the 80 cm^2 surface, 87 drops are deposited giving $\alpha_{\text{drops}} = (10.5 \pm 1)$ %. Note that the drops or the droplets are not perfectly half-sphere and thus the wet surface cannot be deduced only from the water volume, total surface and number of drops. The uniform water layer thickness is deduced from the total

volume and covered surface assuming that the water is evenly distributed below the polycarbonate plate: 0.1 mm.

To discuss the impact of water on the **S** matrix, we must ensure a uniform drops or droplets distribution along the sample, and a large beam radius compared to the drop size and spacing. These two conditions ensure no dependence of the **S** matrix with the beam position. In the J band, the surface illuminated by the beam is 12.6 cm^2 assuming a disk of 2 cm radius. Therefore, the number of illuminated drops is on average 14 while the number of droplets is about 100. Regarding the uniformity of the water deposition, it is well mastered for the drop shape, but more randomly for the droplet shape. For the drop shape, the non-dependence of the S matrix with the beam position shall be ensured by the good uniformity and the sufficiently large number of drops illuminated. In the droplet shape, it shall be by the large number of droplets illuminated: the non-uniformity issues are smoothed out. The measurements were performed up to 10 times for each band and for each shape. In every case, similar behavior was observed and similar fit obtained with the model proposed in section 6.

3.2 Characterization of the wet radome

In order to remove the contribution of the polycarbonate plate from the measured radome covered by the uniform water layer, the plate was characterized alone and going through the **T** matrix transformation, in a fashion similar to the water permittivity extraction from the container (see appendix). Removing the contribution of the polycarbonate plate is not straightforward and requires the exact location of the measured S-parameter reference planes to be known. After the TRL calibration, the measured **S** matrix has a single reference plane : the face of the sample on the side which is not moved during the Line standard measurement in the calibration procedure, namely the left side in Fig. 3.a. Therefore, the measured **S** matrix must be corrected by adding a phase shift corresponding to an air layer with a thickness equal to the total sample thickness h_{tot}. As port-1 is not moved, the corrected **S** matrix, denoted S^c, is calculated as follows:

$$\begin{aligned} S^c_{11} &= S_{11} \\ S^c_{21} &= S_{21}\, e^{-j\beta_0 h_{\mathrm{tot}}} \\ S^c_{12} &= S^c_{21} \\ S^c_{22} &= S_{22}\, e^{-j2\beta_0 h_{\mathrm{tot}}} \end{aligned}$$

where $\beta_0 = 2\pi/\lambda_0$ with λ_0 the wavelength in the air. The obtained $\mathbf{S}^c$ matrix after this initial correction is shown in Fig. 3.b along with the **S** matrix obtained from the modeled radome-water-plate stack. While there is a perfect match in magnitude, only S_{21} presents a good match in phase between the measurement and the expected result. The phase difference between model and measurement in S_{11} and S_{22} is due to a slight mechanical positioning

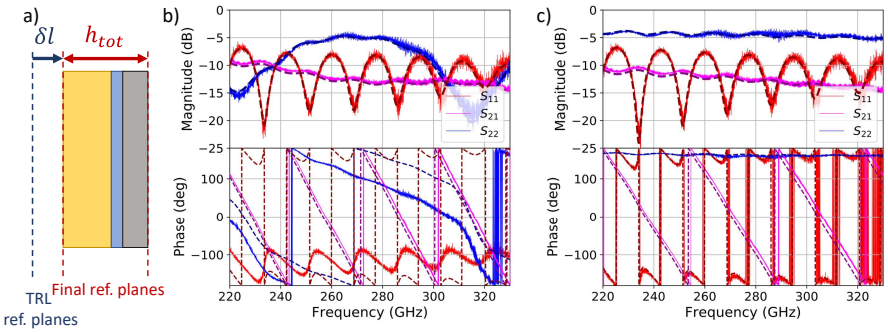

Fig. 3 a) Sample stack under test: PVC radome (in yellow), uniform water layer (in blue) and polycarbonate plate (in grey). The two planes in dashed red are the final reference planes of the S-parameters. The plane in blue is the initial plane for all measured S-parameters after the calibration. b) S-parameters measured in the J band for the radome covered by the thin water film and the polycarbonate plate. The first phase correction is applied. c) The same measurement after the second phase correction and with the contribution from the plate removed. The water is deposited only on the port-2 side. S_{12} is similar to S_{21}.

error of the sample in the TRL calibration reference plane. This type of mechanical error, written δl, is of a few tens of micrometers and is less visible in the Ka or W band, but must be corrected in the J band and beyond. To do so, both S_{11} and S_{22} are multiply by $e^{j\beta_0\delta l}$ and $e^{-j\beta_0\delta l}$ respectively. Once this phase shift is applied to the S-parameters of the radome-water-plate stack, the contribution of the plate can be finally removed. The resulting **S** matrix of the radome-water stack is compared with the model in Fig. 3.c showing a perfect match in both phase and magnitude. This ensure that the uniform water film is indeed of the expected thickness as the water thickness was not a free parameter in the model. Note that, in the Ka band, a uniform water layer on a surface large enough for the measurement with this method was not achievable because of the much larger size of the gaussian beam.

4 Experimental observations

The **S** matrix for the three different shapes of water and the dry radome is shown in Fig. 4 in the W band and Fig. 5 in the J band. The water is deposited only on the port-2 side, therefore S_{22} is the reflection on the water side and S_{11} the reflection on the dry side. S_{12} is not shown as it is equal to S_{21}. The

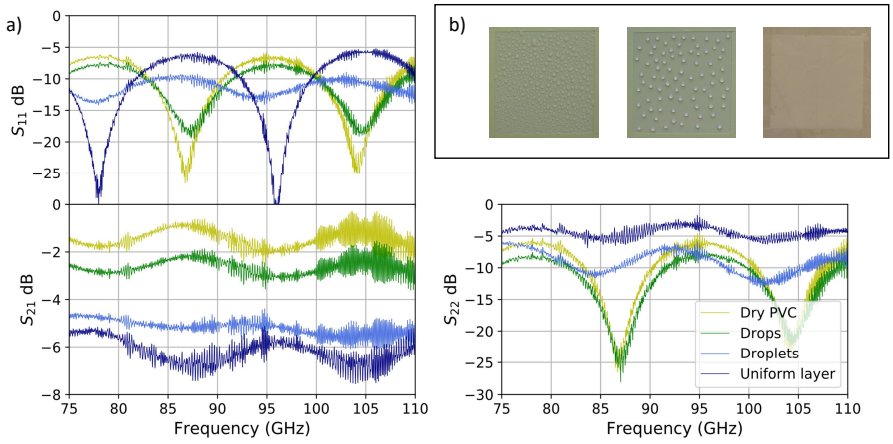

Fig. 4 a) Magnitude of the S-parameters in the W band for the dry radome or the radome covered by the three shapes of water. The water is deposited only on the port-2 side. S_{12} is equal to S_{21}. b) The radome covered by the three different shapes of water: droplets, drops and a uniform layer from left to right.

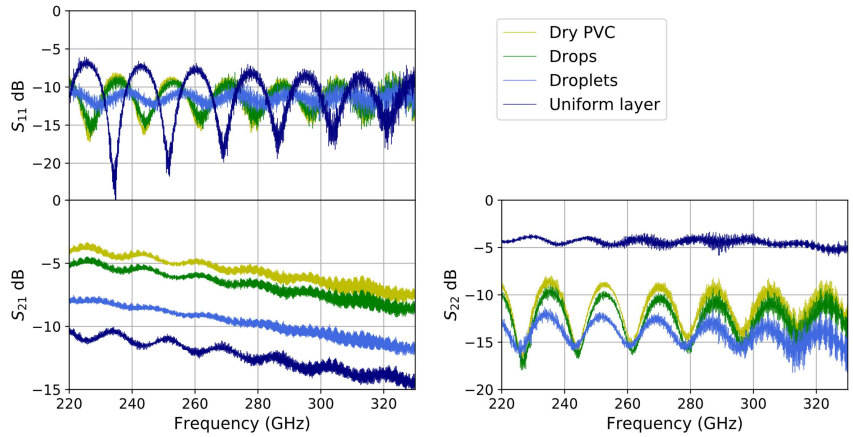

Fig. 5 Magnitude of the S parameters for the dry radome or the radome covered by the three shapes of water in the J band. The water is deposited only on the port 2 side. S_{12} is equal to S_{21}.

multilayer reflection process, named Fabry-Perot interferences, depends on the frequency and the number of interfaces and the thickness of the layers. For

the dry radome, we observe strong variations for S_{11} and S_{22} and weak ripples for S_{21}. Regarding the radome covered by a uniform water layer, S_{11} presents variations similar to the dry case with a resonance frequency shift. On the water side, the reflection coefficient S_{22} is of course higher compared to the dry case. The transmission coefficient S_{21} is reduced overall. We observe that the **S** matrix of the radome covered by drops is overall similar to the dry radome one. There is a slight reduction of the amplitude of the ripples for S_{11}, an average of 1 dB loss in transmission and a reduction of the S_{22} overall magnitude. In the droplet case, the variations for all S-parameters are strongly reduced when compared to the drop water shape and the overall additional loss in transmission is about 3 dB in both the W and the J band. For this constant volume of water, a higher transmission loss is observed for the uniform layer shape: about 4.5 dB in the W band and 7 dB in the J band. The monotonous decrease of the magnitude of S_{21} with frequency in each band is not related to the water as this effect is observed with the dry radome as well. It is due to the frequency dependence of the imaginary part of the PVC's relative permittivity.

The measurement presented in Fig. 6 focuses on the behaviour of the drop and droplet shapes in the Ka and W bands. The amplitude of the ripples for the radome covered by droplets is reduced in the W and the J band but not in the Ka band. This decrease of the ripple amplitude as the frequency increases is more pronounced for S_{21} and S_{11} as compared with S_{22}. The dashed lines in Fig. 6 highlight the frequency dependence due to the imaginary part of the PVC permittivity. They are obtained from an average value of equation 1 applied to the dry radome, with an arbitrary offset for the drops and droplets cases. It is thus observed that, only in the droplets case, the frequency dependence of the transmitted amplitude is not fully due to the PVC dispersion.

5 Discussion

For radar applications, we are mostly interested in the transmission losses through the water-covered radome, namely S_{21}. The measurements are summarized in Fig. 7 over the three frequency bands. The larger the total area covered by water, the greater the losses due to the water layer. This holds true regardless of the frequency and this could be due to transmission through the gap between drops or droplets, as discussed in [13].

A second point of interest for radar applications is the mismatch in the reflection coefficient magnitude between the dry radome and the radome covered by a uniform layer of water (radar side is S_{11} here). As seen for in Fig. 4 and Fig. 5, in the dry radome configuration, the maximum of the reflection coefficient S_{11} corresponds to a minimum in the configuration of a uniform water layer on the radome. This effect adds itself to the absorption through the water layer and can deteriorate further the performances of a radome optimized in dry conditions. This mismatch due to water is once again avoided by reducing the total wet surface: it remains small for the radome covered

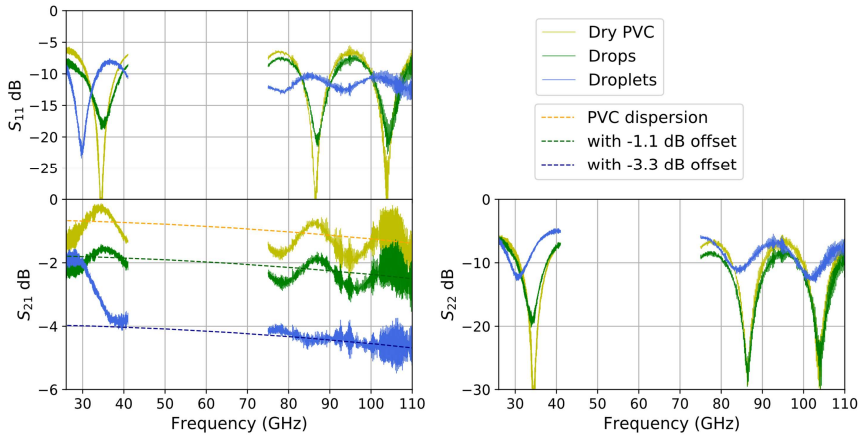

Fig. 6 Magnitude of the S parameters for the dry radome or the radome covered by drops or droplets in the Ka and W band. The same drop distribution was measured in both bands almost simultaneously. The water is deposited only on the port-2 side. S_{12} is similar to S_{21}. Dashed line in S_{21}: average value through a period obtained from equation 1, with an offset for the drops and droplets.

by drops. For applications, how detrimental this effect can be depends on the water thickness and permittivity as the worst case scenario is measured here.

The magnitudes of the S-parameters in the dry radome configuration and the radome covered by a uniform water layer are well understood by (1) and (2) as depicted in Fig. 7 (orange and black dashed lines). The 2-dB difference between the W-band measurement and the model for the uniform water layer is due to measurement performed at a different room temperature leading to a slightly different complex permittivity of the water. By taking this into account, the red dashed curve which better fits the measurement is obtained.

For the drop and the droplet shapes, more complex effects are observed such as: i) the reduction of the amplitude of the ripples in the case of the droplets, which is not observed with the larger drops, ii) the average reflected magnitude on the water-covered side (namely the average value of S_{22}) is smaller in the case of a radome covered with water drops compared to the dry radome case. To predict the behaviour of the radome covered by drops, a simple approach would be to make use of the mixing rules which derive an effective permittivity for the drop layer from the permittivity of water and air [19] (Maxwell-Garnett equation). However these models are only valid if the size of the drops is very small compared to the wavelength. This is not the case in the present experiment as drop diameters range from 0.1 to 4 mm and the wavelength is from 12 mm to 1 mm.

We observed in Fig. 6 that, only in the droplets case, the frequency dependence of the transmitted amplitude is not fully due to the PVC dispersion in the Ka band, namely for the smaller drops at the larger wavelength. From scattering models [7], the frequency dependence of the scattered intensity is expected to change with the R/λ ratio with R the drop radius. If $R \ll \lambda$ Rayleigh scattering is expected and the scattered intensity varies as $1/\lambda^4$. If $R \sim \lambda$, we are in the Mie scattering region and the frequency dependence of the intensity is more complex. As the frequency dependence of the transmission magnitude for the radome covered by drops is fully accounted by the dispersion of the PVC, scattering cannot play an important part in the total signal loss for this water shape. Scattering is not observed in this system because there is a single layer of about 100 drops deposited on the radome, that is, very little scattering spheres as compared for instance to the drops in the air between the radome and the target during a rainfall event.

For the droplet case, there are more scattering spheres of smaller radius. As the frequency decreases towards the Ka band, the wavelength increases and gets closer to the Rayleigh scattering region. The scattering intensity is expected to be smaller and to depend sharply on frequency. It could therefore explain the behaviour of the transmitted intensity for the radome covered by droplets. In the Ka band the scattered intensity is still small as it varies as $1/\lambda^4$, then moving towards the W band, we enter a region where the scattering intensity is stronger but depends less clearly on the frequency. As a result, the frequency dependence of S_{21} simply follows the dispersion of PVC. In other words, only in the Rayleigh scattering region, a frequency dependence other than the one from the PVC dispersion could be observed. Note that the amplitude of the S_{21} ripples are only reduced in the droplet case, in the W and J band. This change in the ripples could be related to scattering as it is only observed in the region of $R \sim \lambda$ where the scattering is strong. Additional measurements would be necessary to investigate further the scattering effects.

6 Compact model for transmission losses

To have a quick estimate of the transmission loss and of the reflectivity increase due to water, we suggest a quasi-empirical model that can take into account the four different cases measured in the present study. The idea is simple and exploits the fact that the measured S-parameters magnitude are an average over the surface illuminated by the gaussian beam. For transmission in the dry radome case, the surface is uniform and therefore $S_{21,\mathrm{dry}}$ is given by (1) for the PVC. For the radome covered by a uniform water layer, $S_{21,\mathrm{uni}}$ is given by cascading the dry PVC with a uniform water layer using the transmission matrix procedure (see appendix) and the relative permittivity of water previously extracted. For the drop or the droplet case, an average is calculated over the surface between the field transmitted through the dry PVC and the field transmitted through the PVC covered by a uniform water layer as follows:

$$|S_{21}| = |(1-\alpha)S_{21,\mathrm{dry}} + \alpha S_{21,\mathrm{uni}}(h_\alpha)| \tag{4}$$

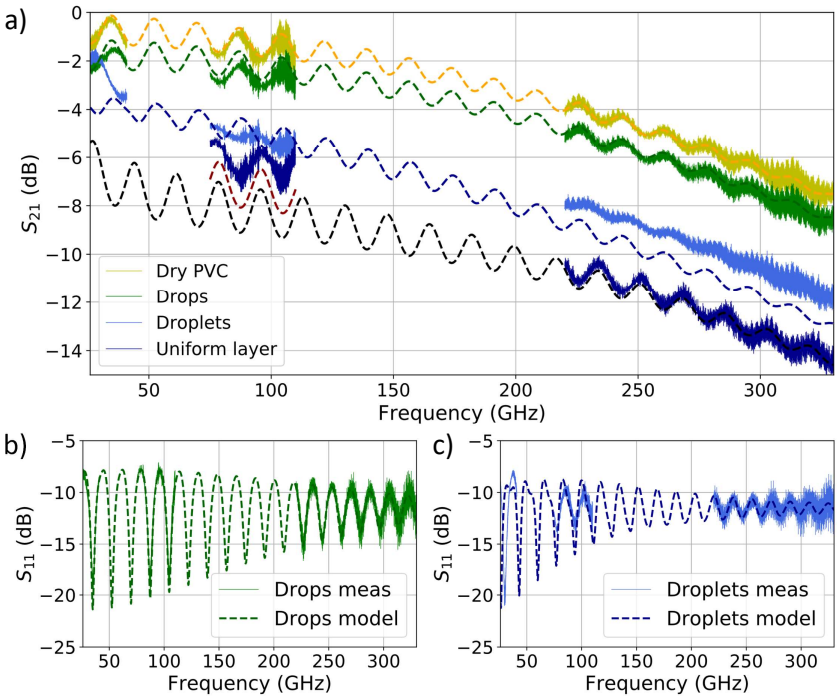

Fig. 7 a) Measured transmitted magnitude through a radome covered by water under different shapes in the Ka, W and J bands. Dashed-lines : the model given by (4) applied for the different values of α (share of wet surface). Measured reflected magnitude towards dry side compared with the model for the b) drops and c) droplets water shapes.

where α is the share of wet surface and $S_{21,\text{uni}}$ is computed for a water thickness h_α such that the total volume of water remains constant as α changes. In other words, we assume that all the drops or droplets are equivalent to a single square-shaped drop, with the measured total wet surface and water volume. A similar equation is used for S_{11}. With this model, the 4 shapes are described: the dry radome with $\alpha = 0$ %, the radome covered by a uniform water layer with $\alpha = 100$ %, the radome with drops with $\alpha = 10.5$ % and the radome with droplets with $\alpha = 40$ %. No additional free parameters are required. The results are shown in Fig. 7.

For the dry radome, a perfect match over the three bands can be observed (S_{11} not shown). The frequency dependence of the transmission is solely due to the dispersion of the permittivity imaginary part as previously mentioned. For the uniform water layer, there is a good match in the J band and the W band if the extracted water permittivity in the W band is taken into account as explained in section II (see red dashed line, S_{11} not shown). In the Ka band, a reliable uniform layer was not possible to achieve over a very large surface with our method. The transmission (Fig. 7.a) and reflectivity (Fig. 7.b) measured for the radome covered by drops is well predicted by the model,

over the full frequency range. The difference in temperature between the W and the J and Ka measurements is less impactful in this case because water has an overall weaker effect. Regarding the droplets, the prediction is not as good as in the drops case for transmission (Fig. 7.a) but remains satisfying in reflectivity for W and J band (Fig. 7.c). There are two main reasons to this imperfect droplets in transmission match: i) α for the droplets is not known as precisely as for the drops because less control over the total wet surface can be achieved while depositing the droplets compared to the drops, ii) the approximation of an uniform squared shape drop made by the model is more detrimental while simulating the droplets because of the large distribution of the droplets radius compared to the narrower radius distribution of the drops.

The proposed model cannot predict the full **S** matrix for all the configurations. Some discrepancies between the model and the measurement in the magnitude of S_{22} for the droplets case and in the phases for the drop and droplet configurations are not perfectly described. Nevertheless, this model can give an estimate of the absorption and reflectivity change by a wet radome for radar applications. The parameters are the permittivity of water and radome, the thickness of the radome, the total volume of water and the share of wet surface. Instead of using the total volume of water, one can use the average water thickness deposited on the radome, which can be obtained from the rain intensity using Gibbel's formula [10]. The share of wet surface will depend on the water flow, the hydrophobicity of the radome surface and its tilt angle. To estimate it, one can use the results presented in [9].

7 Conclusion

S-parameter measurements over a wide frequency range of a radome covered by water have been presented. Three different water shapes with a constant volume and a varying total wet surface were studied. A new method to control a thin water layer was proposed, highlighting the importance of having a good control of the phases of the measured S-parameters. The main result regarding applications is that to limit the signal losses due to water, the total wet surface should be reduced. We propose a compact model that can be used to predict the transmission losses and reflectivity increase for all types of water flow on the radome. The measurements raised questions on the role of scattering in the total extinction due to water. For drops sufficiently large, we found that scattering plays only a minor role. To further investigate this aspect, measurements at lower frequency are of interest. We are currently working on a more complete model describing the behaviour of the millimeter waves going through a surface covered by water drops using the method of moments.

A S to T matrix

The **S** matrix and the **T** matrix are linked by:

$$\mathbf{S} = \begin{bmatrix} \frac{T_{21}}{T_{11}} & T_{22} - T_{12}\frac{T_{21}}{T_{11}} \\ \frac{1}{T_{11}} & -\frac{T_{12}}{T_{11}} \end{bmatrix}$$

$$\mathbf{T} = \begin{bmatrix} \frac{1}{S_{21}} & -\frac{S_{22}}{S_{21}} \\ \frac{S_{11}}{S_{21}} & S_{12} - S_{11}\frac{S_{22}}{S_{21}} \end{bmatrix}$$

The **T** matrix of the liquid inside the container, $\mathbf{T}_{\text{liquid}}$, from the full container measurement is given by:

$$\mathbf{T}_{\text{liquid}} = \mathbf{T}_{\text{A,mod}}^{-\mathbf{1}} \mathbf{T}_{\text{meas}} \mathbf{T}_{\text{B,mod}}^{-\mathbf{1}}$$

where $\mathbf{T}_{\text{meas}}$ is the measured **T** matrix (applying the $S \to T$ transformation) and $\mathbf{T}_{\text{A,mod}}$ ($\mathbf{T}_{\text{B,mod}}$) is the **T** matrix of the panel A (panel B) which is on the port-1 (port-2) side. The matrix of the panels are obtained from the calculated S-parameters using (1) and (2) and the permittivity characterization of each panel. Such that, we do not multiply the noise from several measurements when removing the contribution of the panels.

To extract the **T** matrix of the radome covered by the uniform water film $\mathbf{T}_{\text{PVC+film}}$ from the measurement of the radome-water-plate stack:

$$\mathbf{T}_{\text{PVC+film}} = \mathbf{T}_{\text{meas}} \mathbf{T}_{\text{plate,mod}}^{-\mathbf{1}}$$

where $\mathbf{T}_{\text{meas}}$ is the measured **T** matrix and $\mathbf{T}_{\text{plate,mod}}$ is the **T** matrix of the polycarbonate plate, once again computed from (1) and (2) using the extracted permittivity of the plate and the $S \to T$ transformation. The water and the plate are on the port-2 side.

B Declarations

Ethical approval: not applicable.

Competing interests: the authors declare having no competing interests as defined by Springer, or other interests that might be perceived to influence the results and/or discussion reported in this paper.

Author's contributions: P.B and A.P wrote the main manuscript text and developped the compact model. A.P and D.B developped the bench for quasi-optical measurements and the methods for permittivity extraction. P.B performed the wet radome measurements. All authors reviewed the manuscript.

Funding: not applicable.

Availability of data and materials: the present manuscript contains no materials from third parties.

References

1. Ian F. Akyildiz, Josep Miquel Jornet, and Chong Han. Teranets: ultra-broadband communication networks in the terahertz band. *IEEE Wireless Communications*, 21(4):130–135, August 2014.
2. Ho-Jin Song. Terahertz wireless communications. *IEEE Microwave Magazine*, 22(5):88–998, May 2021.
3. Shizhe Zang, Ming Ding, David Smith, Paul Tyler, Thierry Rakotoarivelo, and Mohamed Ali Kaafar. The Impact of Adverse Weather Conditions on Autonomous Vehicles: How Rain, Snow, Fog, and Hail Affect the Performance of a Self-Driving Car. *IEEE Vehicular Technology Magazine*, 14(2):103–111, June 2019.

4. Jian Gong, Meili Li, and Mingyuan Zhang. Material testing and optimum thickness calculation for automotive millimeter wave radar radome. In *2021 International Conference on Microwave and Millimeter Wave Technology (ICMMT)*, pages 1–3, 2021.
5. Simon Kueppers, Harun Cetinkaya, and Nils Pohl. A compact 120 GHz SiGe:C based 2 × 8 FMCW MIMO radar sensor for robot navigation in low visibility environments. In *2017 European Radar Conference (EURAD)*, pages 122–125, Nuremberg, Germany, October 2017. IEEE.
6. Thi-Hong-Lê Dam, Camille Delfaut, Grégory Houzet, Thierry Lacrevaz, Alejandro Niembro-Martin, Quoc-Bao Duong, Nadège Reverdy-Bruas, and Tan-Phu Vuong. Printed radome for reconfigurable antenna radiation pattern in 5G applications. In *2021 IEEE International Symposium on Antennas and Propagation and USNC-URSI Radio Science Meeting (APS/URSI)*, pages 309–310, 2021.
7. Jie Huang, Yusheng Cao, Xavier Raimundo, Adnan Cheema, and Sana Salous. Rain Statistics Investigation and Rain Attenuation Modeling for Millimeter Wave Short-Range Fixed Links. *IEEE Access*, 7:156110–156120, 2019.
8. Lorenzo Luini, Giuseppe Roveda, Maurizio Zaffaroni, Mario Costa, and Carlo G. Riva. The Impact of Rain on Short ${E}$ -Band Radio Links for 5G Mobile Systems: Experimental Results and Prediction Models. *IEEE Transactions on Antennas and Propagation*, 68(4):3124–3134, April 2020.
9. Jorge L. Salazar-Cerreño, V. Chandrasekar, Jorge M. Trabal, Paul Siquera, Rafael Medina, Eric Knapp, and David J. McLaughlin. A Drop Size Distribution (DSD)-Based Model for Evaluating the Performance of Wet Radomes for Dual-Polarized Radars. *Journal of Atmospheric and Oceanic Technology*, 31(11):2409–2430, November 2014.
10. I. Anderson. Measurements of 20-GHz transmission through a radome in rain. *IEEE Transactions on Antennas and Propagation*, 23(5):619–622, September 1975.
11. Xiaoming Liu, Lu Gan, and Bin Yang. Millimeter-wave free-space dielectric characterization. *Measurement*, 179:109472, July 2021.
12. N. Chen, R. Gourova, O.A Krasnov, and A. Yarovoy. The influence of the water-covered dielectric radome on 77GHz automotive radar signals. In *2017 European Radar Conference (EURAD)*, pages 139–142, Nuremberg, October 2017. IEEE.
13. Fatemeh Norouzian, Rui Du, Edward G. Hoare, Peter Gardner, Costas Constantinou, Mikhail Cherniakov, and Marina Gashinova. Low-THz Transmission Through Water-Containing Contaminants on Antenna Radome. *IEEE Transactions on Terahertz Science and Technology*, 8(1):63–75, January 2018.
14. Paul F. Goldsmith. *Quasioptical Systems: Gaussian Beam Quasioptical Propogation and Applications*. Wiley–Blackwell, 1997.
15. Daniel Bourreau, Alain Peden, and Sandrick Le Maguer. A Quasi-Optical Free-Space Measurement Setup Without Time-Domain Gating for Material Characterization in the W-Band. *IEEE Transactions on Instrumentation and Measurement*, 55(6):2022–2028, December 2006.
16. Constantine A Balanis. *Advanced engineering electromagnetics*. John Wiley & Sons, 2012.
17. Daniel Bourreau and Alain Peden. Solid and Non-Solid Dielectric Material Characterization for Millimeter and Sub-Millimeter Wave Applications. In *2020 50th European Microwave Conference (EuMC)*, pages 909–912, Utrecht, Netherlands, January 2021. IEEE.
18. Hans J. Liebe, George A. Hufford, and Takeshi Manabe. A model for the complex permittivity of water at frequencies below 1 THz. *International Journal of Infrared and Millimeter Waves*, 12(7):659–675, July 1991.
19. Ari Sihvola. Mixing rules with complex dielectric coefficients. *Subsurface sensing technologies and applications*, 1(4):393–415, 2000.